Catalysis Today 151 (2010) 354–361

Contents lists available at ScienceDirect

Catalysis Today

journal homepage: www.elsevier.com/locate/cattod

Nature and spatial distribution of sulfur species in a sulfated barium-based commercial lean NO_x trap catalyst[☆]

Jae-Soon Choi [a,*], William P. Partridge [a], Michael J. Lance [b], Larry R. Walker [b], Josh A. Pihl [a], Todd J. Toops [a], Charles E.A. Finney [a], C. Stuart Daw [a]

[a] Fuels, Engines, and Emissions Research Center, Oak Ridge National Laboratory, P.O. Box 2008, MS-6472, Oak Ridge, TN 37831-6472, USA
[b] High Temperature Materials Laboratory, Oak Ridge National Laboratory, P.O. Box 2008, MS-6068, Oak Ridge, TN 37831-6068, USA

ARTICLE INFO

Article history:
Available online 18 February 2010

Keywords:
Lean NO_x trap
NO_x storage/reduction
Oxygen storage capacity
Sulfation
Barium
Spatial distribution

ABSTRACT

We report observations of the nature and spatial distribution of sulfur species on a sulfated Ba-based commercial lean NO_x trap (LNT) catalyst. The monolithic catalyst was sulfated in a bench flow reactor during 60/5-s NO_x-storage/reduction cycling to achieve a total sulfur loading of 3.4 g L^{-1} of catalyst. Washcoat composition, structure and sulfur distribution were analyzed with electron probe microanalysis, X-ray diffraction, Raman spectroscopy, X-ray photoelectron spectroscopy, and temperature-programmed reduction. The most significant washcoat elements of catalytic relevance were Pt, Pd, Rh, Ba, Ce, Zr, Mg, Al, and these were present mainly in four distinct domains: (i) Mg/Al mixed oxide with Pt, Ce; (ii) Al oxide with Rh, Pd; (iii) Ce/Zr mixed oxide with Pt, Pd, Ba (high Ba content); (iv) Ce/Zr mixed oxide with Pt, Pd, Ba (low Ba content). Sulfur was present in the form of sulfates that decreased in concentration along the LNT axis from front to back. Barium showed the highest sulfur affinity leading to a plug-like axial progression of its sulfation. The sulfation of Al, Mg/Al, and Ce/Zr oxides was less vigorous with a more axially dispersed and less penetrating front.

1. Introduction

Lean NO_x traps (LNTs, also known as NO_x storage/reduction or NSR catalysts) are being implemented for NO_x after treatment in lean-burn vehicles [1,2]. To overcome the 3-way catalyst's inability to reduce NO_x under lean (i.e., oxygen-rich) exhaust conditions, LNTs incorporate NO_x-storage materials (alkali or alkaline-earth metals) into typical 3-way catalyst formulations (precious metals, oxygen storage materials, supports) [3,4]. LNTs store NO_x as nitrates or nitrites during normal fuel-lean engine operation (storage or trapping step) and release and reduce the stored NO_x via intermittent short fuel-rich excursions (regeneration step).

Despite the remarkable progress made in the development of LNTs, significant technical improvement is still necessary to meet ever more stringent emission regulations and realize broad deployment. Sulfur poisoning is a particularly important and difficult issue to address. Sulfur, present in the engine exhaust mainly as SO_2, can be oxidized to SO_3 over the precious metal sites of the LNT, and react with the alkali or alkaline-earth metal components to form sulfates. As the NO_x-storage components (Ba, K) have greater affinity for SO_3 than NO_2, LNT catalysts progressively lose their NO_x-storage capacity over time when exposed to exhaust sulfur. As a result, high-temperature reductant-rich exhaust conditions are periodically created to "desulfate" the catalyst and regain its NO_x-storage performance. Desulfation typically requires temperatures significantly higher than the normal LNT operation, which can entail thermal aging with permanent activity loss [5,6]. A primary challenge is therefore to develop more sulfur-resistant LNTs and more effective desulfation strategies which minimize the thermal aging and fuel penalty associated with high-temperature desulfation.

Meeting this challenge will require a better understanding of the LNT chemistry; in particular, with respect to how sulfur interacts with different components of a fully formulated LNT catalyst over both space and time. Spatial distribution of the relevant reactions is especially important because it directly determines the integral performance of LNT devices. As mentioned above, in addition to NO_x-storage materials (Ba, K), practical LNTs contain various other components such as platinum group metals (PGM: Pt, Pd, Rh), supports (Al_2O_3, TiO_2, CeO_2), oxygen storage capacity (OSC: CeO_2–ZrO_2), and additives (La, Fe) [4]. Sulfur can bind to more than one component [7–9] and thereby affect various

---

[☆] *Notice*: This submission was sponsored by a contractor of the United States Government under contract DE-AC05-00OR22725 with the United States Department of Energy. The United States Government retains, and the publisher, by accepting this submission for publication, acknowledges that the United States Government retains, a nonexclusive, paid-up, irrevocable, worldwide license to publish or reproduce the published form of this submission, or allow others to do so, for United States Government purposes.

[*] Corresponding author. Tel.: +1 865 946 1368; fax: +1 865 946 1354.
E-mail address: choijs@ornl.gov (J.-S. Choi).

0920-5861/$ – see front matter © 2010 Elsevier B.V. All rights reserved.
doi:10.1016/j.cattod.2010.01.016

LNT functions. Moreover, even in sulfur-free operation, LNT chemistry changes along the catalyst length; for example, more nitrates are accumulated near the front [10–14]. Sulfur impacts on the axially evolving chemistry of multi-component LNTs are not well understood, but important for the development of advanced LNT systems.

In previous studies on a Ba-based commercial LNT catalyst, we monitored the evolution of catalytic performance with increasing sulfation level [15,16]. Detailed intra-catalyst gas analyses revealed that sulfur poisons NO_x-storage–reduction function along the catalyst axis in a plug-like manner at 325 and 400 °C. In contrast, sulfur deactivates the oxygen storage function much less aggressively, leading to an axially more dispersed sulfation front and only partial loss of OSC in the sulfated zone. These findings were used to explain the increased NH_3 selectivity with sulfation. That is, the plug-like poisoning of NO_x-storage sites (mainly Ba) resulted in an axial displacement of the NH_3-forming NO_x-storage–reduction zone and a concommitant shortening of the downstream oxygen storage-only zone, thereby reducing the downstream oxidation of NH_3 that managed to slip unreacted from the NSR zone.

In the present study, we performed detailed physicochemical characterization of the same LNT catalyst to determine the nature and spatial distribution of sulfur species and by doing so refine our interpretation of the LNT performance trend [15,16]. In the following discussion, we show that the characterization results confirm the sulfation trends deduced previously [15,16] and provide additional details regarding the contributions of distinct compositional domains in the washcoat as depicted in Fig. 1.

2. Experimental

2.1. Catalyst and sulfation procedure

A commercial gasoline direct injection (GDI) LNT manufactured by Umicore (washcoated honeycomb cordierite monolith; 97 cells per cm^2) was in the focus of the present study. This particular catalyst had been adopted as a representative commercial LNT for study in the Crosscut Lean Exhaust Emissions Reduction Simulations (CLEERS) research community [17]. Briefly, the catalyst contains magnesium, aluminum, cerium, zirconium, and barium as major components. Other elements of significance were platinum, palladium, rhodium, lanthanum, iron, and titanium. The bulk concentrations of Pt, Pd, Rh, Ba, Ce, and S as determined by ICP-AES are reported in Ref. [16]. The bulk density of the unsulfated catalyst (mass of washcoat monolith substrate per volume) is ca. 570 g L^{-1} and the total surface area (substrate + washcoat) was determined to be 27.1 $m^2\,g^{-1}$ by N_2 adsorption using the BET method. More details about this catalyst can be found in previously published work: bench-reactor evaluation [15,16,18–20], engine-platform evaluation [21], kinetic models [22,23], DRIFTS analyses [16,23], sulfation [15,16], and NH_3 selectivity [15,16,18,21–23].

The 2.1-cm-diameter and 7.4-cm-long core evaluated in Ref. [15,16], was used in this study. The sample was wrapped in Zetex insulation tape and inserted into a horizontal quartz reactor tube (2.2-cm inside diameter). The reactor tube was heated by an electric furnace, and simulated exhaust gas mixtures were prepared using pressurized gas bottles (ultra high purity grade, Air Liquide). The gases were metered with mass flow controllers (Unit Instruments Series 7300, Kinetics Electronics) and preheated before entering the quartz reactor. Water was introduced by a peristaltic cartridge pump (Cole-Parmer) to a heated zone, vaporized and added to the simulated exhaust mixture. A rapid switching 4-way valve system was used to alternate between the lean and rich gas mixtures (60/5-s lean/rich cycling). The lean-phase mixture contained 300 ppm NO, 10% O_2, 5% H_2O, 5% CO_2 and N_2 balance, and the rich-phase mixture contained 3.4% H_2, 5% H_2O, 5% CO_2 and N_2 balance.

During lean/rich cycling at 400 °C and a gas hourly space velocity (GHSV) of 30,000 h^{-1}, 40 ppm SO_2 was added into the feed stream for 2 h to achieve a total sulfur input of 3.4 g L^{-1} of catalyst. Following the sulfur exposure, the system was allowed to equilibrate for 0.5 h under lean/rich cycling without SO_2. This sulfation process resulted in virtually complete sulfur uptake with negligible sulfur breakthrough as confirmed by independent experiments with another equivalent sample using two sulfur analyzers (API-Model 100A: UV fluorescence SO_2, and AMETEK-Western Research Series 900: non-dispersive UV SO_2, H_2S).

2.2. Catalyst characterization

For catalyst characterization, the sulfated sample was sliced, perpendicular to the catalyst length, into four equal segments and each segment was sliced into two equal hemicylinders along the catalyst length. These segments were analyzed by electron probe microanalysis (EPMA), X-ray diffraction (XRD), Raman spectroscopy, X-ray photoelectron spectroscopy (XPS), and temperature-programmed reduction (TPR). Fig. 2 summarizes this sample preparation procedure.

A Jeol JXA-8200 SuperProbe electron probe microanalyzer was used to determine the elemental composition of catalyst washcoat. Samples were prepared for analyses by mounting in epoxy and polishing the inlet side of each section. Three types of EPMA measurements were carried out: (i) 10-μm-spot-size line analyses along a diagonal line of washcoat cross-sections; (ii) elemental mapping over entire washcoat cross-sections; (iii) high-resolution point analyses on various local domains (grains) on one of the washcoat cross-sections mapped in (ii). The high-resolution analysis was performed by measuring for 40 s at each point (400 times longer than the elemental maps; and as a result, the signal-to-noise ratio was 20 times higher). Due to the heterogeneous and porous nature of

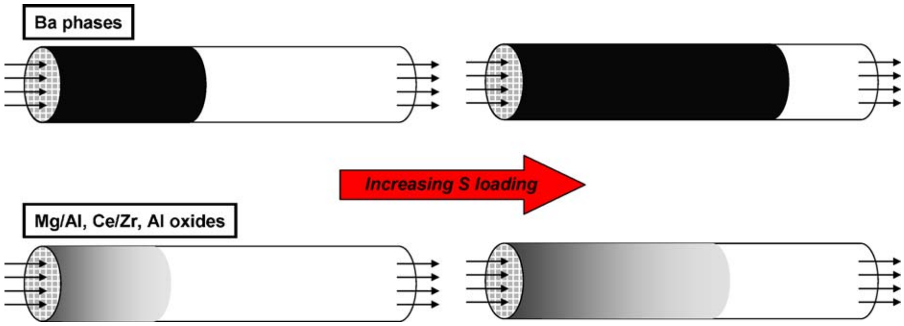

Fig. 1. Conceptual depiction of the axial progression of sulfation for different LNT components. Darker color indicates higher degree of sulfation for a given component.

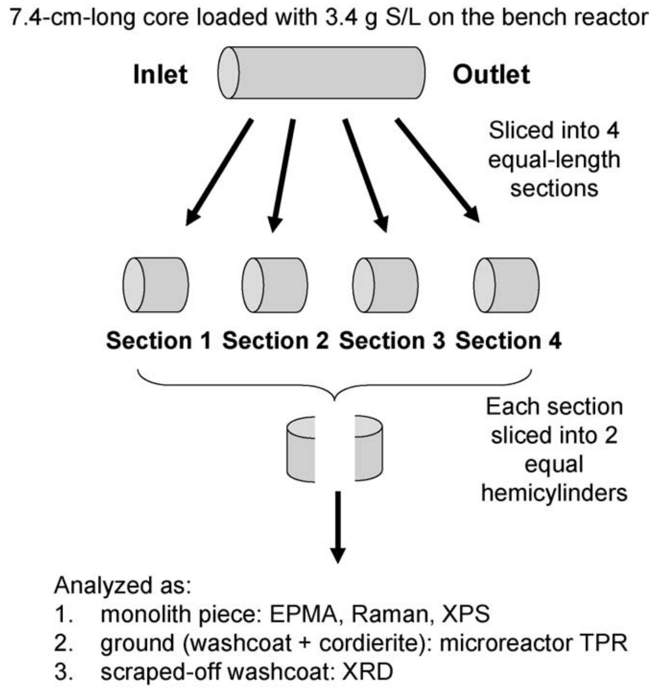

Fig. 2. Procedure for catalyst sectioning and sample preparation for catalyst characterization.

the washcoat, the spot size could not be accurately determined for the measurement types (ii) and (iii). However, it was almost certainly smaller (approximately one cubic micron) than the typical grain size of the constituent phases measured in the point measurements. In addition, the elemental weight percent was determined by comparing the sample X-ray intensity to a standard sample. This comparison was based on the assumption that the probed volume was homogeneous, which was invalid in this study. Therefore, the compositional data is likely accurate to not less than a few percent and should be viewed more as a relative comparison between different measurements (of identical microstructure) than as an absolute measurement.

Elemental spatial cross-correlation analyses were performed with the obtained EPMA elemental maps which represent the relative intensity (in wt.%) of a given element at each pixel (probe-spot location) in an x–y grid. For each pair of element images X and Y, after zeroing any negative values (noises), a cross-correlation coefficient was calculated:

$$C_{X,Y} = \langle X(i,j)\cdot Y(i,j)\rangle / \sqrt{\mathrm{var}(X)\cdot\mathrm{var}(Y)}$$

where i and j are pixel indices and $\langle\cdot\rangle$ is expected value; the denomimator nomalizes C in $[-1, +1]$ by scaling by the individual variances (var), and X and Y are centered to have zero mean. Values of C close to 1 indicate strong correlation (i.e., have high coincidence of elements X and Y being found together at the same probe location), and negative values indicate anti-correlation (i.e., have low coincidence).

X-ray diffraction patterns were collected using a PANalytical XRD with $Cu_{k\alpha}$ radiation. To minimize interferences from the cordierite substrate, the washcoat was scraped off from the catalyst sample for analyses.

Raman spectra were collected with a Dilor XY800 Raman Microprobe using an Ar^+ laser operating at 5145 Å. The spot size was 10 μm. A total of 100 spectra were collected along the length of the monolith and averaged.

A Thermo Scientific k-alpha X-ray photoelectron spectrometer using an $Al_{k\alpha}$ X-ray source was used to collect both survey and high-resolution scans. The measurement spot size was 200 μm and was focused on the center of one channel of each monolith. Energy was detected with a hemispherical electron analyzer multichannel plate (MCP).

Temperature-programmed reduction of both intact monolith and power samples was used to characterize the thermal stability of the sulfates at different axial locations of the sulfated catalyst. The monolith was exposed to a flowing mixture of 1% H_2, 5% H_2O, 5% CO_2, balance N_2 (GHSV = 30,000 h^{-1}) while the furnace temperature was raised from 400 to 700 °C at 5 °C min^{-1} and then maintained at 700 °C for ca. 1 h. Concentrations of H_2S and SO_2 were monitored at the reactor outlet with the two S analyzers described above.

Powder TPR samples were prepared by grinding each axial section (i.e., including both washcoat and cordierite substrate) and ca. 130 mg of each sample was loaded in a microreactor. The microreactor feed gas consisting of 1% H_2, 5% CO_2 and 5% H_2O in Ar was initially established in the microreactor bypass stream while the furnace was heated to 400 °C with the reactor sealed in Ar. The feed gas flow rate was held constant at 100 $cm^3\ min^{-1}$ (STP), which roughly corresponded to a GHSV of 50,000 h^{-1}. Once the target temperature and flow were achieved, the feed gas was switched from the bypass to the microreactor, and the temperature was ramped to 1000 °C at 5 °C min^{-1}. The effluent gas stream passed through a downstream oxidation catalyst reactor which converted the H_2S (only S product) into a thermodynamically equilibrated SO_2/SO_3 mixture [24] whose composition was then determined by an SO_2 analyzer (API-Model 100A).

3. Results and discussion

3.1. Composition and structure of the washcoat

Fig. 3 is a backscattered electron image of the washcoat cross-section (i.e., along the thickness plane) of the sulfated catalyst (Section 1: front quarter) in a corner of a flow channel. The cordierite substrate and open flow channel can be seen in the upper-right and lower-left corners, respectively. As revealed by Fig. 3, the overall composition of washcoat was radially uniform. This was also confirmed by an EPMA line scan with a spot diameter of 10 μm measured diagonally from the cordierite corner to the washcoat surface (Fig. 4). Additional scans at different locations along the monolith axis also indicated a uniform washcoat distribution (results not shown). The average washcoat composition for Section 1 estimated by averaging over 20 data points is reported in Table 1 (both wt.% and at.%).

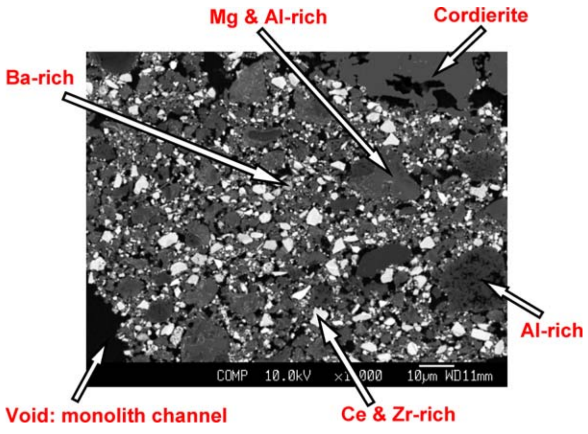

Fig. 3. Backscattered electron image of a sulfated commercial lean NO_x trap catalyst sample (Section 1); a washcoat cross-section (i.e., in the thickness plane) in a corner of a flow channel is shown.

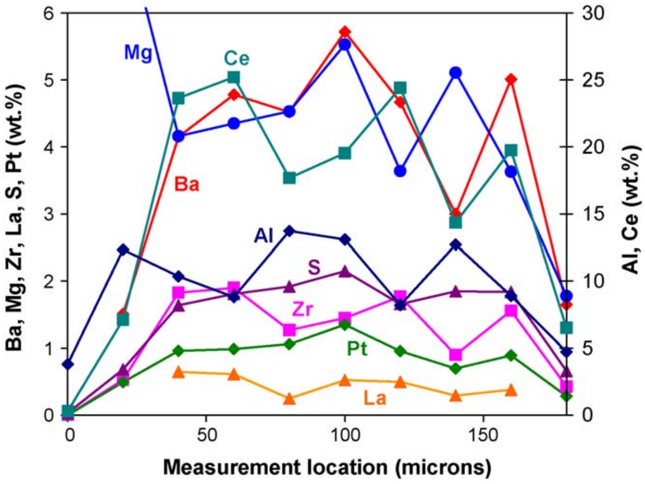

Fig. 4. Radial distribution of washcoat composition measured by EPMA over a sulfated commercial lean NO_x trap catalyst sample (Section 1) at 20 micron increments diagonally from cordierite–washcoat interface with a spot diameter of 10 μm.

Table 1
Global concentration (weight and atomic %) of washcoat metal components estimated from EPMA of the sample Section 1[a,b].

	Pt	Pd	Ba	Ce	Zr	Mg	Al	La	O	S
wt.%										
Average	1.5	0.4	6.2	30.4	2.3	7.1	16.6	0.7	32.3	2.7
Stdev.	0.4	0.0	1.0	5.1	0.5	1.0	2.9	0.2	2.9	0.3
at.%										
Average	0.2	0.1	1.4	6.7	0.8	8.8	18.4	0.1	60.9	2.6
Stdev.	0.1	0.0	0.3	1.6	0.2	0.7	2.2	0.1	1.9	0.3

[a] Values obtained by averaging data over 20 measurement points; Rh was not measured.

[b] The C, N, Si contaminants attributable to sample preparation (epoxy, cordierite) were eliminated and the concentrations were normalized to 100% total assuming that these 10 components represent the majority of the washcoat content.

Based on a mass balance between the bulk Ce content (11.9 wt.% from Ref. [16]) and washcoat Ce content (30.4 wt.% from Table 1), we estimate the total washcoat loading to be ca. 223 g L^{-1} compared to the total LNT bulk density of ca. 570 g L^{-1}. Subsequently, we estimate the approximate loadings (in g L^{-1}) of major oxides based on wt.% values in Table 1: CeO_2 (83); ZrO_2 (7); BaO (15); MgO (26); and Al_2O_3 (70). We caution that these loading values should be considered as rough estimates and are presented here for relative comparison of different components, since we did not perform a rigorous EPMA calibration with respect to matrix effects. The total BaO loading estimated by EPMA washcoat measurements (15 g L^{-1}) is ca. 83% of the loading value estimated by bulk ICP-AES analyses (18 g L^{-1}, based on data in Ref. [16]).

At smaller scales, the composition of this LNT catalyst is clearly non-uniform. For instance, in Fig. 3 there are regions where particular elements are visibly concentrated as indicated by arrows: Mg and Al-; Al-; Ba-; and Ce and Zr-rich areas. The nature of these regions of clustered elements is further revealed in Fig. 5, which quantifies cross-correlations among different pairs of elements. In Fig. 5, greater confidence is associated with the strongly correlated (+1) and anti-correlated (−1) values relative to correlations near zero; experimental (e.g., different noise levels for different elements) and calculation (e.g., different concentration levels for different elements) artifacts not addressed in this analysis may have a greater impact on correlations far from ±1.

Fig. 5a indicates a strong correlation between Mg and Al (see coefficient close to 1). In contrast, Mg had clear anti-correlations with Ce and Zr. Such a strong and exclusive correlation between Mg and Al indicates that these components were intimately related as a single compound (i.e., Mg/Al mixed oxide) with minor stand-alone Mg and/or Al phases. On the other hand, Ce showed a strong correlation with Zr in Fig. 5b (i.e., Ce/Zr mixed oxide), but anti-correlations with Mg and Al. Zirconium is a well known additive to Ce-based oxygen storage material providing improved redox behavior and thermal stability [25]. The Mg/Al and Ce/Zr mixed oxides were therefore present in the washcoat mainly as two separate domains. Fig. 5b also indicates positive correlation among Ce, Zr, Ba, Pt, and Pd, suggesting that Ce/Zr was not only an OSC-component, but also the support for "active LNT ingredients" (Ba, Pt, Pd). Benefits of using CeO_2 as support, instead of more conventional Al_2O_3, have been reported as minimizing Pt sintering [26,27], enhancing low-temperature NO_x-storage–reduction performance [27–29], and improving S tolerance [27]. Fig. 5c and d also supports the positive correlations among Ce, Zr, Ba, Pt, and Pd.

The four compositionally distinct washcoat domains, whose representative grains are indicated by arrows in Fig. 3, were further analyzed by performing additional EPMA at much higher signal-to-noise ratios (high resolution) than used for Figs. 4 and 5. The results, summarized in Table 2, corroborate the above-mentioned interpretations and reveal extra details. Indeed, the individual domains showed compositions significantly different from the global washcoat composition (Table 1). For instance, a domain rich in Mg/Al mixed oxide with an atomic Mg/Al ratio of ca. 1/3 (assuming all Mg and Al belong to the mixed oxide) is obvious. Improved sulfur tolerance [30] and catalytic performance [30,31] have been reported by incorporating Mg/Al mixed oxide to "active" LNTs. The Mg/Al mixed oxide contained Pt but no significant amount of Pd or Rh. Some Ce was also present in the Mg/Al domain; Ce addition has been reported to enhance redox properties of this type of mixed oxides [31,32].

A second type of domain was composed of Al oxide where Rh was exclusively located. A smaller amount of Pd was also present, but Pt was absent. This Al-rich phase exhibited photo-stimulated luminescence spectra typical of γ-Al_2O_3 (spectra not shown). The remaining two domain types (Ba-rich and Ce, Zr-rich) both consisted of Ce, Zr, Ba, Pt, and Pd, but the Ba and Ce contents were very different. The Ba-rich domain contained similarly high amounts of Ba (15.7 at.%) and Ce (12.1 at.%), while the other domain contained less than 1.4 at.% of Ba and 25.6 at.% of Ce. The atomic Ce/Zr ratio of both domains was ca. 6/1. Other minor elements, present in each of the four domains but not described above, are assumed to be either additional dopants or contaminants due to the sample preparation procedure.

The XRD pattern in Fig. 6 collected on Section 1 provides additional evidence regarding the four washcoat domains. Besides the peaks due to cordierite, which was unintentionally included in the sample during the washcoat-scraping-off process, two major oxide phases are obvious: Ce and Mg/Al mixed oxides. The absence of clear features associated with Al oxide in Fig. 6 suggests that the majority of the washcoat Al was associated with Mg with a small percentage of stand-alone Al (alumina: "Al-rich" domain shown in Fig. 3 and Table 2). Moreover, despite the domains with high Ba concentration, the Ba was invisible by XRD; therefore the Ba appears to have mainly been in amorphous phases. The peaks at 40° and 66° in Fig. 6 are unknown at this time.

Raman spectroscopy (Section 1) in Fig. 7 further supports the significance of CeO_2 phase in the washcoat as well as sulfates and carbonates, while the XPS survey scan (Section 1) in Fig. 8a confirms the presence of major elements Ce, Zr, Ba, Mg, Al, and S on the sulfated catalyst surface.

In summary, the catalyst studied in this work had washcoat that was axially and radially uniform at global scales, but which was resolvable into four compositionally distinct local domains at smaller scales. The major constituents of these domains were

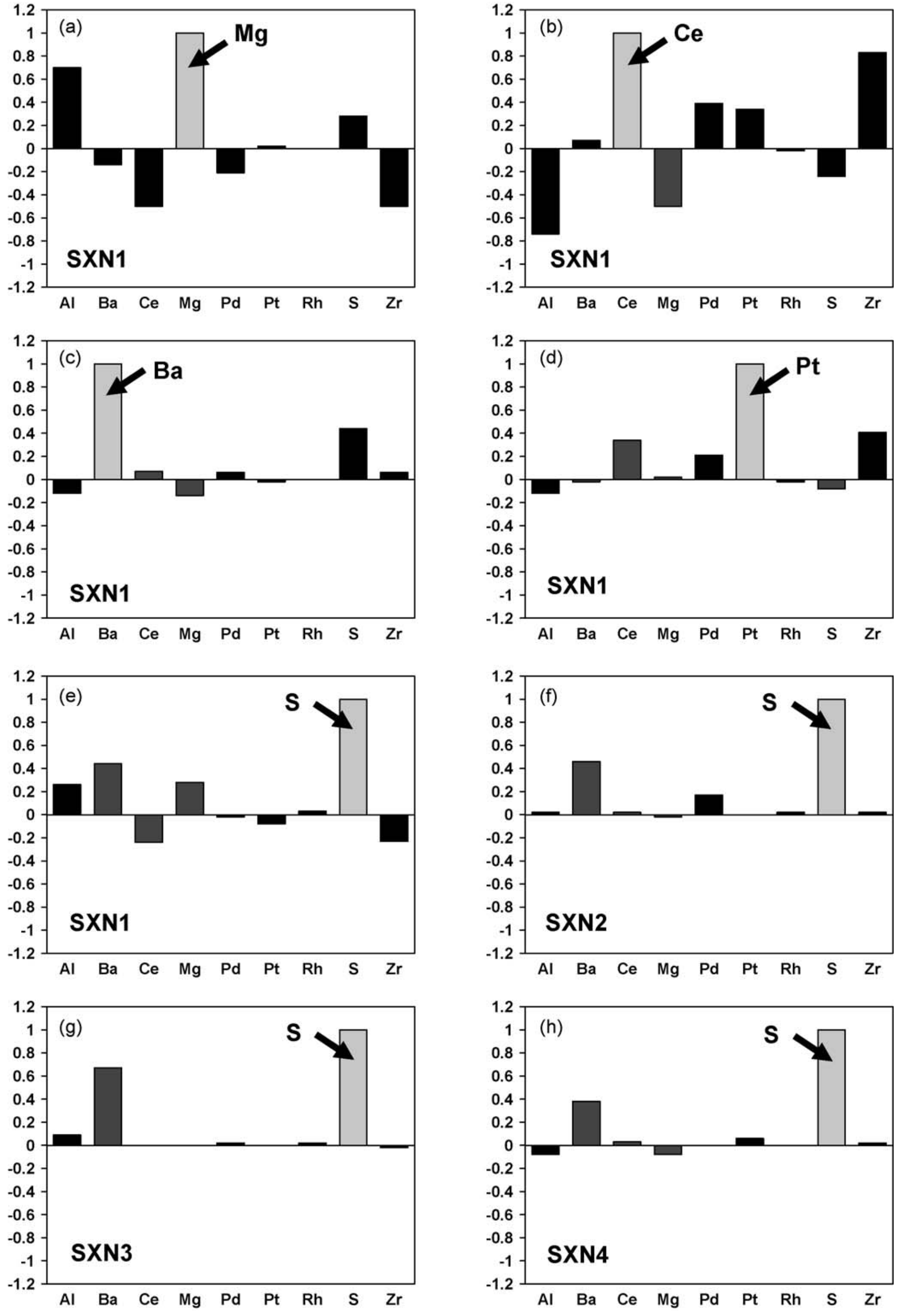

Fig. 5. Statistical analyses of elemental cross-correlations based on EPMA maps of LNT washcoat cross-sections. In each component-specific panel, the *x*-axis indicates the elements being compared while the *y*-axis indicates the cross-correlation intensity (coefficient), with 1 and −1 indicating the highest and the lowest correlations, respectively. Bright bars represent self-correlation (for visual reference) and dark bars cross-correlation between different components.

(i) Mg/Al mixed oxide with Pt, Ce;
(ii) Al oxide with Rh, Pd;
(iii) Ce/Zr mixed oxide with Pt, Pd, Ba (high Ba content);
(iv) Ce/Zr mixed oxide with Pt, Pd, Ba (low Ba content).

3.2. Nature and spatial distribution of sulfur species

In line with our previous DRIFTS analyses on the same LNT sample [16], both Raman spectroscopy (Section 1) in Fig. 7 and high-resolution XPS scan (Section 2) in Fig. 8b confirm that the sulfur was present on the catalyst as sulfates. However, the measurements were not sensitive enough to discriminate among different types of sulfates (e.g., Ba vs. Ce).

The EPMA results (Table 2, Fig. 5e) reveal positive correlations between sulfur and various elements indicating the presence of different sulfate types which were not differentiated by DRIFTS, Raman, and XPS. In fact, BaO [4–9,33], CeO_2 [7,27,34], and $MgAl_2O_4$ [30,35,36] components are all known to store sulfur. As expected,

Table 2
Composition of four distinct washcoat domains estimated from high-resolution EPMA of the sample Section 1. The C, N, Si contaminants due to sample preparation were eliminated and the concentrations were normalized to have 100% total assuming that these 10 components represent the majority of the washcoat content.

at.%	Pt	Pd	Rh	Ba	Ce	Zr	Mg	Al	O	S
(i) Mg, Al-rich domain (averaged over 5 different measurement points)										
Average	0.2	0.0	0.0	0.0	0.9	0.0	10.6	34.2	52.8	1.2
Stdev.	0.2	0.0	0.0	0.1	0.5	0.0	1.0	1.4	2.2	0.8
(ii) Al-rich domain (averaged over 3 different measurement points)										
Average	0.0	0.2	1.0	0.5	0.2	0.0	2.0	40.5	53.2	2.4
Stdev.	0.0	0.1	0.3	0.4	0.2	0.0	1.1	2.6	0.4	1.0
(iii) Ba-rich domain (averaged over 3 different measurement points)										
Average	0.4	0.2	0.0	15.7	12.1	1.9	2.1	5.6	54.8	7.3
Stdev.	0.2	0.1	0.0	8.1	6.4	1.0	0.4	1.6	1.1	2.0
(iv) Ce, Zr-rich domain (averaged over 12 different measurement points)										
Average	0.6	0.4	0.0	1.4	25.6	4.3	1.1	3.3	61.1	2.1
Stdev.	0.2	0.2	0.0	0.6	3.9	1.3	0.7	2.4	2.7	1.2

the most basic component of the catalyst, Ba, showed the highest affinity for S (Fig. 5e–h). In terms of S storage by domain type, the order was Ba-rich ≫ Al-rich > Ce/Zr-rich > Mg/Al-rich (Table 2).

By comparing the relative S contents of different domains in the context of their respective elemental composition, we can further deduce the relative S affinity of individual LNT components. First, the Ba-rich domain stored 3.5 times as many S atoms as Ce/Zr-rich domain (Table 2). As these two domains contain similar types of elements with a major difference being Ce/Ba ratio, the observed 3.5 times storage difference clearly indicates a much higher S affinity of Ba compared to Ce/Zr. It is thus reasonable to expect that even within the Ce/Zr-rich domain the small amount of Ba (1.4 at.%) stored incoming S more vigorously than Ce/Zr during sulfation. Then only about 0.7 at.% S would have been bound to the non-Ba portion of the domain (mainly Ce/Zr).

The Mg/Al-rich domain did not contain any measurable Ba, so its S content of 1.2 at.% would have been associated mainly with Mg/Al mixed oxide. The Al-rich domain also contained some Ba (0.5 at.%) and again reasonably assuming preferential Ba sulfation, ca. 1.9 at.% S would have been bound to other components, mainly Al oxide. In summary, the S affinity of different major LNT components appears therefore to be in the order of BaO ≫ Al_2O_3 > Mg/Al mixed oxide > Ce/Zr mixed oxide.

Overall, the cross-correlation with S was the strongest in Section 1 (the 1st quarter of the monolith, Fig. 5e) and the weakest in Section 4 (the last quarter of the monolith, Fig. 5 h). As described in Experimental, the EPMA elemental maps used to calculate the cross-correlation coefficients represent the relative intensity of a given element in wt.%. As the loadings of the washcoat components were virtually unchanged along the catalyst length, more elements having positive correlation with S toward the catalyst front indicates that Section 1 had the highest total S. This observation is consistent with our previous DRIFTS and elemental analyses which indicated the sulfur to be the highest near the catalyst inlet and the lowest near the outlet [16]. The S correlation with Ba was uniquely strong relative to all other washcoat components over the entire LNT length (Fig. 5e–h), further supporting the outstanding affinity of Ba for S.

The TPR of the sulfated monolith sample produced a complex profile of H_2S – the only reduction product observed with 1% H_2 used in the present study (Fig. 9a) – confirming that several surface S species indeed resulted from the sulfation process. Although more work is necessary for a refined peak deconvolution and identification, the peaks found in Fig. 9a match reasonably well with previously reported desulfation temperatures of different compounds. First, the low-temperature feature around 525 °C could be assigned to CeO_2 [34], Al_2O_3 [6,9,37], and $MgAl_2O_4$ [35,36]. The Ba in Pt/Ba/Al_2O_3 has been shown to have different types of sulfates, for example, surface and harder-to-desulfate bulk sulfates [6,9,37]. The two higher temperature features around 595 and 695 °C are within these reported temperature ranges. Recently, we have performed a series of TPR experiments on

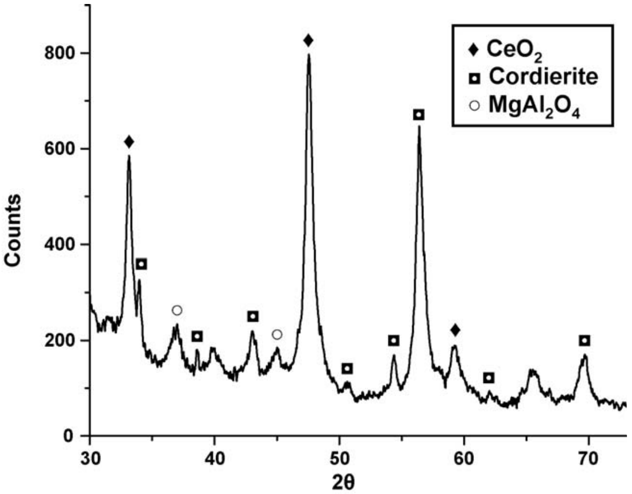

Fig. 6. XRD pattern of washcoat sample scraped off of the sulfated commercial lean NO_x trap (Section 1).

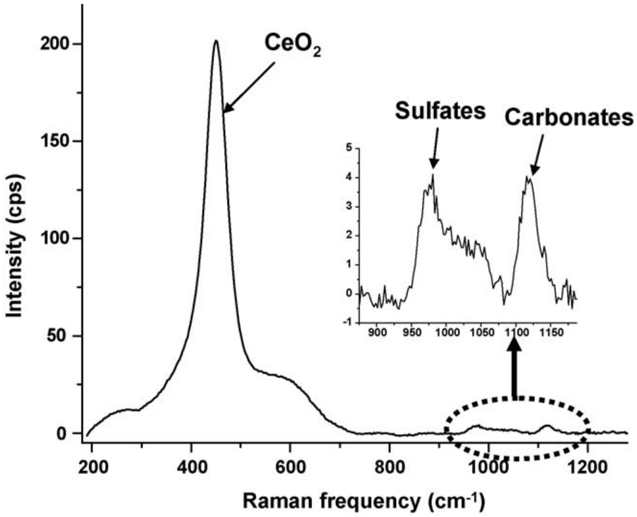

Fig. 7. Raman spectrum of washcoat surface from flow-channel wall of the sulfated commercial lean NO_x trap (Section 1).

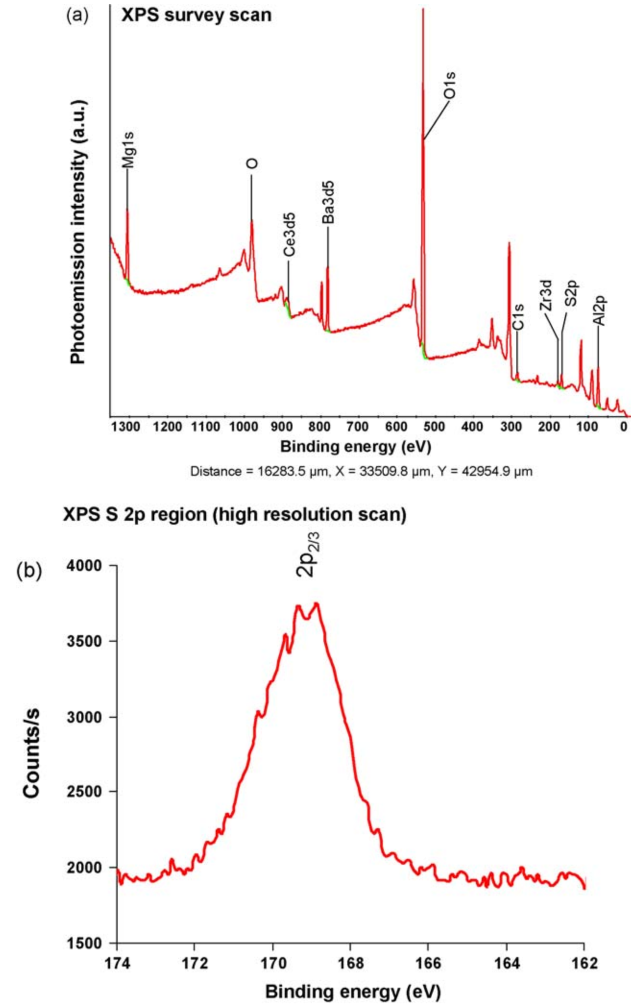

Fig. 8. XPS (a) survey-scan spectrum of Section 1 (the main transition for each element is labeled; the unlabeled peaks are all minor transitions for the same elements) and (b) high-resolution S 2p spectrum of Section 2 of the sulfated commercial lean NO_x trap.

various LNT components including Al_2O_3, Pt/Al_2O_3, $MgAl_2O_4$, $Pt/MgAl_2O_4$, $Pt/CeO_2–ZrO_2$, and $Pt/Ba/CeO_2–ZrO_2$. The details of this study on model systems will be published in a separate paper [38], but the results generally support the above-mentioned peak assignments. One notable additional information from Ref. [38] is that $Pt/MgAl_2O_4$ and Pt/Al_2O_3 can form high-temperature sulfates in addition to low-temperature ones.

To assess the quantity and axial distribution of these different S species, TPR was performed for powder samples from each quarter section of the catalyst (Fig. 9b). Again, several S species (low and high-temperature features) were apparent. From the axial evolution of the overall TPR profiles, it is clear that the S loading was the highest at the catalyst front and continually decreased along the length. The low-temperature features (attributed to sulfur on Ce/Zr, Mg/Al and Al oxides) decreased steadily along the catalyst length and the last quarter showed virtually no low-temperature features.

In contrast, the high-temperature features (attributed mainly to surface and bulk Ba sulfates) remained high up to the 3rd quarter section and decreased abruptly between the 3rd and 4th sections. The Section 4 contained only high-temperature features with negligible low-temperature counterparts. The axial trend in Fig. 9b is in good agreement with that shown in Fig. 5e–h (EPMA) and our previous results obtained with spatially resolved gas analysis [15,16] and elemental analysis [16], which can be summarized as the following: the axial progression of Ba sulfation was more plug-like and penetrating than that of Al, Mg/Al, and Ce/Zr oxide sulfation.

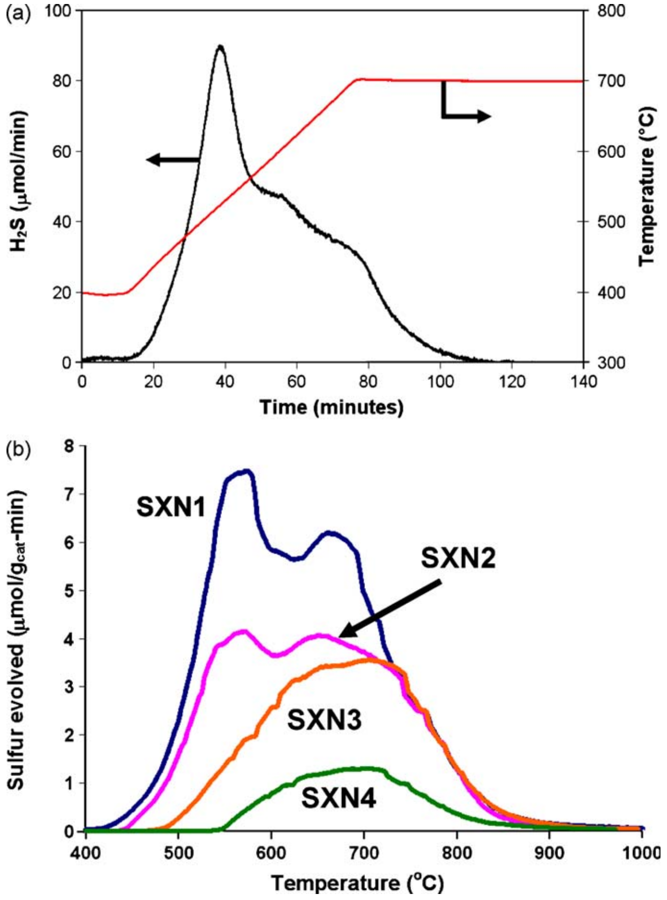

Fig. 9. TPR of the sulfated commercial lean NO_x trap in flowing 1% H_2, 5% H_2O, 5% CO_2, and inert balance: (a) whole 7.4-cm-long monolith core and (b) four individual sections in powder form.

3.3. *Implication of the observed washcoat sulfur distribution in the evolution of catalyst performance*

As described in Introduction, our previous study based on spatially resolved performance evaluation suggested more plug-like and axially penetrating sulfation of the NO_x-storage-component compared to that of the OSC-component of the catalyst. The detailed characterization results reported in the present study clearly support and clarify this conjecture and the details of the sulfation chemistry (Fig. 1). Due to its high basicity, Ba most aggressively captured the incoming S. As the Ba in each zone approached S saturation, the S front marched successively down the axis in a plug-like fashion. As a point of clarification, we suggest that "S saturation" in this context refers to the easily accessible Ba sites relevant to fast NO_x-storage/reduction cycling. It also appears that there were some Ba atoms associated with less accessible "bulk" sites that were much more constrained by solid phase diffusion [9]. It may be these bulk sites that accounted for the Ba/S atomic ratio of ca. 2/1 for the Ba-rich domain in Table 2.

Beyond the Ba sulfation front, the catalyst remained almost free of S contamination. Therefore, at temperatures where only a portion of the catalyst was needed to achieve a high NO_x conversion [15,16], the S-free downstream portion of the catalyst could store and reduce a high percentage of incoming NO_x until axial progression of Ba sulfation reached a critical level. On the other hand, the plug-like progression of Ba sulfation displaced the NH_3-forming NO_x-storage–reduction zone downstream [15,16]. As a result, the OSC-only zone downstream of the NSR zone was gradually shortened thereby decreasing the extent of NH_3 oxidation by OSC. Hence, NH_3 breakthrough continually increased with increasing sulfation.

Other catalyst components such as Al, Mg/Al, and Ce/Zr were also sulfated, but less efficiently due to their lower sensitivity to S. In other words, sulfur broke through each axial zone after completely sulfating its Ba component, but with only partial sulfation of Al, Mg/Al, and Ce/Zr oxides. This led to more dispersed sulfation fronts with respect to these oxides, which appears to be consistent with the pattern of OSC-function degradation observed in Ref. [15,16]. Nonetheless, Al, Mg/Al and Ce/Zr oxides captured significant amounts of incoming S. About twice as many S atoms were loaded in Section 1 as what would have been necessary for full sulfation of the Ba present (see Table 1). In other words, these non-Ba oxides captured a large portion of the incoming S and acted as “S-traps” delaying the progression of Ba sulfation [30]. Additional possible roles and interplays among these oxides in the functioning of the LNT are not clearly understood at this time and require further study.

4. Conclusions

We performed detailed characterization of a sulfated commercial lean NO_x trap using EPMA, XRD, Raman, XPS, and TPR to determine the nature and spatial distribution of sulfur species. The results have been interpreted in the context of NO_x conversion performance measurements published previously to further clarify the roles that different sulfur species played in the evolution of LNT performance. Key findings in the present study were

- The washcoat of the studied LNT is composed mainly of four compositionally distinct domains: (i) Mg/Al mixed oxide with Pt, Ce; (ii) Al oxide with Rh, Pd; (iii) Ce/Zr mixed oxide with Pt, Pd, Ba (high Ba content); (iv) Ce/Zr mixed oxide with Pt, Pd, Ba (low Ba content).
- Ba was the most strongly sulfating component leading an axially plug-like sulfation and poisoning of NO_x-storage–reduction function.
- Sulfation of Al, Mg/Al and Ce/Zr oxides was less efficient than Ba sulfation, leading to more dispersed sulfation fronts, partial oxide sulfation, and partial inhibition of the oxygen storage–reduction function.
- The amount of S stored on non-Ba oxides was significant and therefore Al, Mg/Al, and Ce/Zr oxides acted as S-traps, delaying the axial progression of Ba sulfation.
- This study demonstrates the complex nature of a practical commercial LNT and helps to understand mechanisms by which sulfation affects local chemistry distributions and LNT performance.
- Further research is needed to develop improved LNT designs with enhanced performance. Areas of particular importance include: (1) the detailed roles of Al and Mg/Al oxides; and (2) sulfur impact on PGM reactivity.

Acknowledgments

This research was sponsored by the U.S. Department of Energy, Office of Energy Efficiency and Renewable Energy, Vehicle Technologies Program, with Ken Howden and Gurpreet Singh as the Program Managers. We thank Dr. Owen Bailey at Umicore for assistance in obtaining the commercial LNT catalyst used in this study. The authors are also grateful to colleagues at ORNL for useful discussions and experimental help, in particular Dr. Harry Meyer for the XPS and Mr. Nathan Ottinger for the powder-sample TPR measurements.

References

[1] B.J. Stroia, N.W. Currier, J. Li, R.D. England, J.W. Bush, H. Hess, SAE Technical Paper, 2008 2008-01-0769.
[2] M.V. Twigg, Appl. Catal. B 70 (2007) 2–15.
[3] N. Miyoshi, S. Matsumoto, K. Katoh, T. Tanaka, J. Harada, N. Takahashi, K. Yokota, M. Sugiura, K. Kasahara, SAE Technical Paper (1995), 950809.
[4] W.S. Epling, L.E. Campbell, A. Yezerets, N.W. Currier, J.E. Parks II, Catal. Rev. Sci. Eng. 46 (2004) 163–245.
[5] S. Poulston, R.R. Rajaram, Catal. Today 81 (2003) 603–610.
[6] S. Elbouazzaoui, E.C. Corbos, X. Courtois, P. Marecot, D. Duprez, Appl. Catal. B 61 (2005) 236–243.
[7] H. Mahzoul, L. Limousy, J.F. Brilhac, P. Gilot, J. Anal. Appl. Pyrol. 56 (2000) 179–193.
[8] S. Matsumoto, Y. Ikeda, H. Suzuki, M. Ogai, N. Miyoshi, Appl. Catal. B 25 (2000) 115–124.
[9] D.H. Kim, J. Szanyi, J.H. Kwak, T. Szailer, J. Hanson, C.M. Wang, C.H.F. Peden, J. Phys. Chem. B 110 (2006) 10441–10448.
[10] B. West, S. Huff, J. Parks, S. Lewis, J.-S. Choi, W. Partridge, J. Storey, SAE Technical Paper, 2004 2004-01-3023.
[11] J.-S. Choi, W.P. Partridge, C.S. Daw, Appl. Catal. A 293 (2005) 24–40.
[12] J.-S. Choi, W.P. Partridge, W.S. Epling, N.W. Currier, T.M. Yonushonis, Catal. Today 114 (2006) 102–111.
[13] K. Aftab, J. Mandur, H. Budman, N.W. Currier, A. Yezerets, W.S. Epling, Catal. Lett. 125 (2008) 229–235.
[14] R.D. Clayton, M.P. Harold, V. Balakotaiah, Appl. Catal. B 84 (2008) 616–630.
[15] J.-S. Choi, W.P. Partridge, C.S. Daw, Appl. Catal. B 77 (2007) 145–156.
[16] J.-S. Choi, W.P. Partridge, J.A. Pihl, C.S. Daw, Catal. Today 136 (2008) 173–182.
[17] http://www.cleers.org (website last visited 15.09.09).
[18] J.A. Pihl, J.E. Parks II, C.S. Daw, T.W. Root, SAE Technical Paper, 2006 2006-01-3441.
[19] W.S. Epling, A. Yezerets, N.W. Currier, Catal. Lett. 110 (2006) 143–148.
[20] W.S. Epling, A. Yezerets, N.W. Currier, Appl. Catal. B 74 (2007) 117–129.
[21] J. Parks, B. West, M. Swartz, S. Huff, SAE Technical Paper, 2008 2008-01-0448.
[22] R.S. Larson, V.K. Chakravarthy, J.A. Pihl, C.S. Daw, SAE Technical Paper, 2006 2006-01-3446.
[23] R.S. Larson, J.A. Pihl, V.K. Chakravarthy, T.J. Toops, C.S. Daw, Catal. Today 136 (2008) 104–120.
[24] L. Kylhammar, P.-A. Carlsson, H.H. Ingelsten, H. Grönbeck, M. Skoglundh, Appl. Catal. B 84 (2008) 268–276.
[25] J. Kašpar, P. Fornasiero, M. Graziani, Catal. Today 50 (1999) 285–298.
[26] M. Casapu, J.-D. Grunwaldt, M. Maciejewski, A. Baiker, S. Eckhoff, U. Göbel, M. Wittrock, J. Catal. 251 (2007) 28–38.
[27] J.H. Kwak, D.H. Kim, J. Szanyi, C.H.F. Peden, Appl. Catal. B 84 (2008) 545–551.
[28] Y. Ji, T.J. Toops, M. Crocker, Catal. Lett. 119 (2007) 257–264.
[29] Y. Ji, J.-S. Choi, T.J. Toops, M. Crocker, M. Naseri, Catal. Today 136 (2008) 146–155.
[30] D.L. Guttridge, J. Li, M.S. Chattha, R.J. Kudla, W.L.H. Watkins, U.S. Patent 6,607,704 (2003).
[31] L.M. Ruwisch, U. Göbel, J. Theis, R. Domesle, U.S. Patent 6,858,193 (2005).
[32] J.S. Yoo, A.A. Bhattacharyya, C.A. Radlowski, Appl. Catal. B 1 (1992) 169–189.
[33] F. Rohr, S.D. Peter, E. Lox, M. Kögel, A. Sassi, L. Juste, C. Rigaudeau, G. Belot, P. Gélin, M. Primet, Appl. Catal. B 56 (2005) 201–212.
[34] P. Bazin, O. Saur, J.C. Lavalley, G. Blanchard, V. Visciglio, O. Touret, Appl. Catal. B 13 (1997) 265–274.
[35] M. Waqif, O. Saur, J.C. Lavalley, Y. Wang, B.A. Morrow, Appl. Catal. 71 (1991) 319–331.
[36] J.-A. Wang, C.-L. Li, Appl. Surf. Sci. 161 (2000) 406–416.
[37] X. Wei, X. Liu, M. Deeba, Appl. Catal. B 58 (2005) 41–49.
[38] N.A. Ottinger, T.J. Toops, J.A. Pihl, J.T. Roop, J.-S. Choi, W.P. Partridge, to be submitted.